nature materials

LETTERS

PUBLISHED ONLINE: 16 NOVEMBER 2015 | DOI: 10.1038/NMAT4478

Spatially orthogonal chemical functionalization of a hierarchical pore network for catalytic cascade reactions

Christopher M. A. Parlett[1], Mark A. Isaacs[1], Simon K. Beaumont[2], Laura M. Bingham[2], Nicole S. Hondow[3], Karen Wilson[1] and Adam F. Lee[1]*

The chemical functionality within porous architectures dictates their performance as heterogeneous catalysts[1]; however, synthetic routes to control the spatial distribution of individual functions within porous solids are limited. Here we report the fabrication of spatially orthogonal bifunctional porous catalysts, through the stepwise template removal and chemical functionalization of an interconnected silica framework. Selective removal of polystyrene nanosphere templates from a lyotropic liquid crystal-templated silica sol–gel matrix, followed by extraction of the liquid crystal template, affords a hierarchical macroporous–mesoporous architecture. Decoupling of the individual template extractions allows independent functionalization of macropore and mesopore networks on the basis of chemical and/or size specificity. Spatial compartmentalization of, and directed molecular transport between, chemical functionalities affords control over the reaction sequence in catalytic cascades[2,3]; herein illustrated by the Pd/Pt-catalysed oxidation of cinnamyl alcohol to cinnamic acid. We anticipate that our methodology will prompt further design of multifunctional materials[4–6] comprising spatially compartmentalized functions.

Multifunctional nanomaterials are ubiquitous in diverse technological applications spanning energy[7], the environment and health[8], to information storage and communication[9]. Synergy between chemically distinct functionalities within porous architectures in particular underpins new magnetic[5] or optical devices, and heterogeneous catalysts[2]. Limited spatial patterning of select materials has been achieved in three dimensions at the submicrometre scale, for example through vapour deposition of aligned carbon nanotubes[10] or two-photon excitation of hydrogels over planar substrates[11], or through biogenic routes[12]. Such approaches respectively incorporate only a single chemically distinct function, require optically transparent and photoresponsive materials, or impart a poor degree of ordering and limited thermochemical stability. Ordered two-dimensional arrays of monometallic or metal/oxide bifunctional nanocrystals have been prepared as model catalysts using electron lithography[13] and drop-casting[14] respectively, but afford extremely low surface areas with co-located active sites. Hence, there are no synthetic routes able to control either the nanoscale spatial distribution, or the communication between, individual functions within three-dimensional porous solids.

A hierarchically ordered macroporous–mesoporous SBA-15 silica framework was synthesized through a new lyotropic true liquid crystal templating route (see Methods), adapting literature methodology[15–17], in which a Pluronic P123 block co-polymer surfactant-templated mesoporous silica network was formed through the acid hydrolysis of tetraethoxyorthosilane around an ordered array of unfunctionalized polystyrene colloidal nanospheres (scanning electron microscopy (SEM) and polydispersity index <0.1 by dynamic light scattering, Supplementary Fig. 1), as illustrated in Fig. 1a. The judicious combination of polar P123 mesopore and nonpolar polystyrene macropore templates facilitates their subsequent independent extraction by means of different polarity solvents. Exclusive extraction of the polystyrene macropore template was unsuccessful through conventional calcination (or toluene reflux) protocols, owing to simultaneous combustion (or dissolution) of the P123 mesopore template. However, a new sub-ambient toluene extraction protocol achieved >95% selective polystyrene removal as evidenced by TEM and porosimetry (Fig. 1b and Supplementary Fig. 2 respectively). The resulting 20 $m^2 g^{-1}$ material comprised empty macropores formed/abutted by surfactant template-filled mesoporous silica (Fig. 1b), permitting selective hydrophobization of the macropore network with octyl groups through reaction of triethoxyoctylsilane with exposed surface silanols (Fig. 1c), confirmed by porosimetry and contact angle measurements (Supplementary Fig. 3). Removal of the P123 surfactant template from within the mesopores was facile under methanol reflux (Supplementary Fig. 4) resulting in a fully detemplated hierarchical bimodal architecture (Fig. 1d) containing (interconnected) hydrophobic 350 nm macropores and hydrophilic 3.5 nm mesopores. The total surface area of 300 $m^2 g^{-1}$ was consistent with reports for macroporous SBA-15 prepared using high-temperature template decomposition, and indeed low-angle X-ray diffraction confirmed a *p6mm* hexagonal arrangement of ordered mesoporous channels. Conventional wet impregnation of this high-area porous material with an aqueous metal salt (H_2PtCl_6), followed by a mild (100 °C) reduction under molecular H_2, yielded chloride-free, face-centred cubic metal Pt nanoparticles (NPs) of 2.2 nm mean diameter confined within the mesopores (Fig. 1e). This spatial localization of nanoparticulate Pt was possible only because of the preceding macropore hydrophobization, which directed the water-dispersed platinum precursor away from the octyl-grafted macropores (Supplementary Fig. 5). Finally, oleylamine-capped, 5.6 ± 0.8 nm colloidal Pd NPs (ref. 18; Supplementary Fig. 6) were introduced exclusively into the macropores; their diameter preventing access to the smaller mesopores (Fig. 1f).

[1]European Bioenergy Research Institute, Aston University, Birmingham B4 7ET, UK. [2]Department of Chemistry, University of Durham, Durham DH1 3LE, UK. [3]Institute for Materials Research, University of Leeds, Leeds LS2 9JT, UK. *e-mail: A.F.Lee@aston.ac.uk

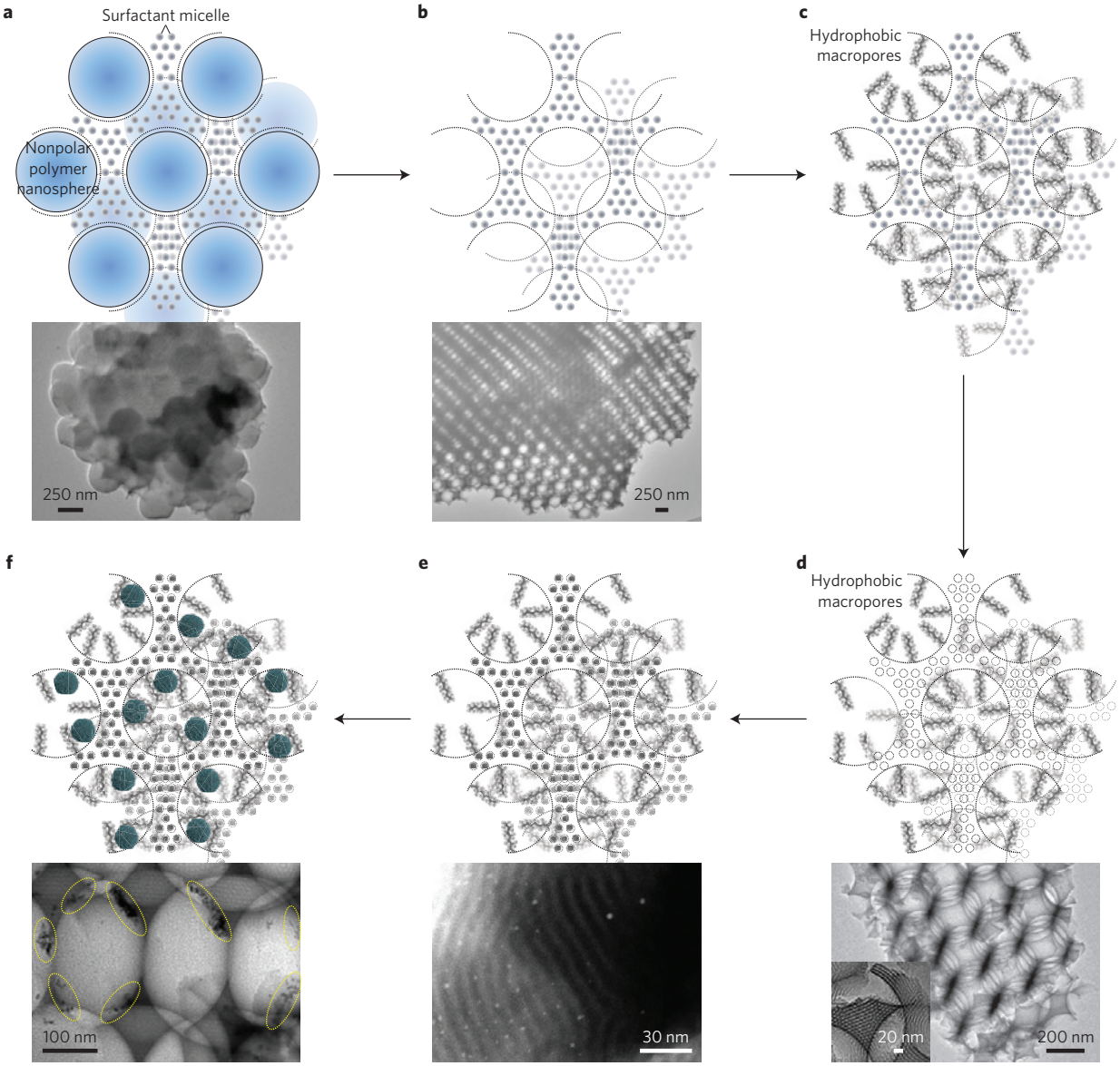

Figure 1 | Synthetic strategy for spatially orthogonal functionalization of hierarchical architectures. a,**b**, Illustrations and bright-field TEM images of parent polystyrene colloidal nanospheres encapsulated within a P123-templated SBA-15 silica network (**a**), and the ordered macroporous framework after selective removal of the polystyrene macropore template by means of toluene reflux (**b**). **c**, Illustration of selective hydrophobization of the macropore framework by triethoxyoctylsilane. **d**, Illustration and bright-field TEM image of ordered hydrophobized macropores and (inset) ordered mesopores following P123 extraction under methanol reflux. **e**, Illustration and HAADF-STEM image of mesopore channels selectively functionalized with Pt NPs through aqueous impregnation and reduction. **f**, Illustration and bright-field TEM image of hydrophobic macropores selectively functionalized with monodispersed 5.6 ± 0.8 nm colloidal oleylamine-stabilized Pd NPs (highlighted in yellow).

Spatial compartmentalization of small Pt NPs within the hydrophilic mesopores, and larger Pd NPs within the hydrophobic macropores, was verified by high-angle annular dark-field scanning transmission electron microscopy (HAADF-STEM) imaging and energy-dispersive spectroscopy (EDX) analysis (Fig. 2) and additional SEM/DF-STEM imaging (Supplementary Figs 7 and 8). *Z*-contrast imaging and line profile analysis through cross-sections of the ordered mesoporous silica framework spanning two macropores (Fig. 2a,b) provide compelling evidence for partitioning of the two metals, with Pt observed only within the mesopores and Pd at the macropore perimeter, and NPs localized within the mesopores affording stronger contrast as anticipated for heavier Pt scatterers (Fig. 2c). Particle size distributions for the spatially orthogonal bimetallic material in Fig. 2d also reveal a bimodal distribution of NPs, with well-defined maxima at 2.4 and 5.5 nm, superimposable with those observed for monometallic Pt or Pd analogues prepared according to the synthetic route in Fig. 1, and consistent with Pd particle sizes from X-ray diffraction (Supplementary Fig. 9). Area-averaged EDX compositions of mesopores and macropores in Fig. 2e affirmed the presence of Pt solely within the former and Pd within the latter. Detailed textural analysis (Supplementary Table 1) confirmed that colloidal Pd incorporation had minimal impact on BET (Brunauer–Emmett–Teller)/mesopore surface areas or mesopore volume, congruent with selective functionalization of macropores; in contrast, Pt wet impregnation significantly lowered these same properties congruent with selective functionalization of mesopores.

Cascade reactions are sequential chemical transformations in which the starting substrate undergoes a reaction whose product becomes the substrate for the next step, and so on, until

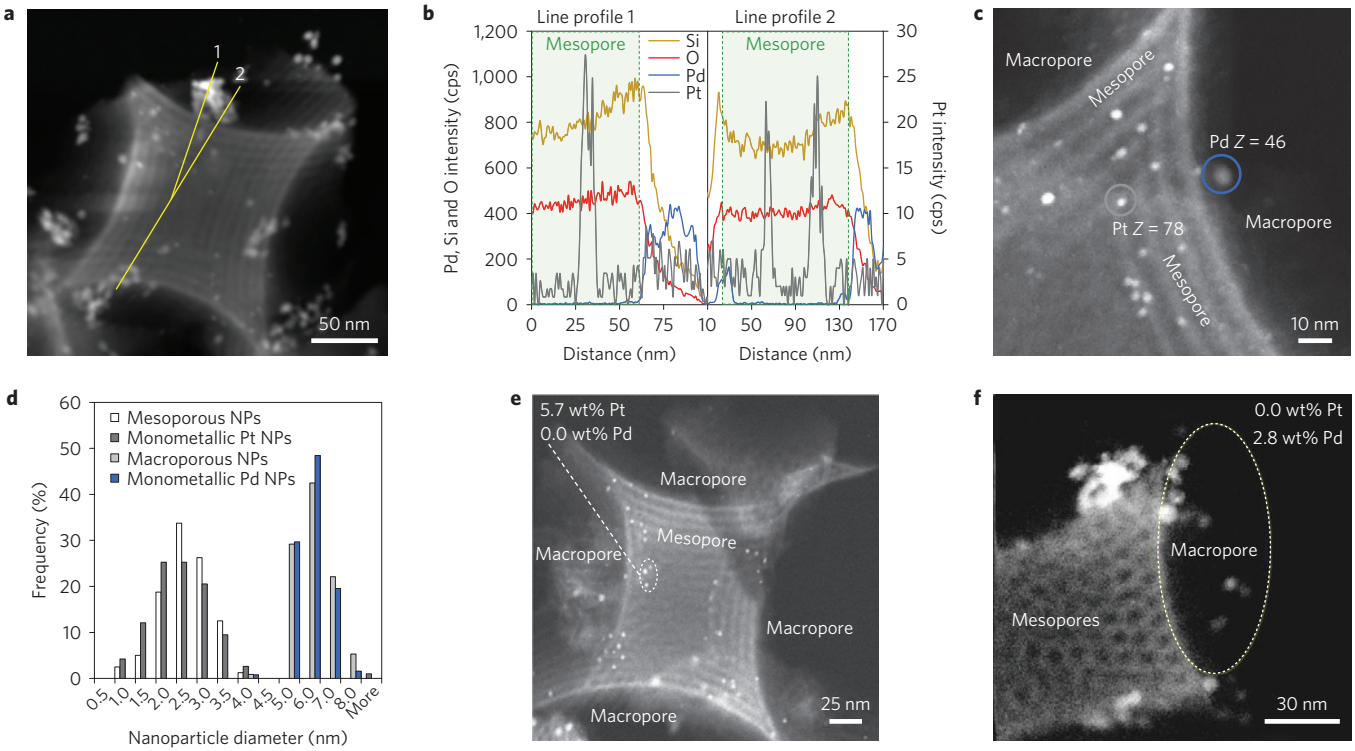

Figure 2 | Visualization of spatially orthogonal Pd and Pt NPs. a, HAADF-STEM of NPs distributed across a section of the mesoporous SBA-15 framework surrounded by macropores. **b**, Cross-sectional EDX compositions of the mesoporous SBA-15 framework intersecting either one (1) or two (2) macropores depicted in **a**. **c**, High-resolution HAADF-STEM image highlighting stronger contrast of smaller, mesopore-confined Pt NPs. **d**, Particle size distributions of monometallic and bimetallic hierarchically ordered macroporous–mesoporous SBA-15 demonstrating selective functionalization of macropores with large Pd NPs and mesopores with small Pt NPs. **e**,**f**, Elemental mapping of mesopores (macropores) showing exclusive Pt (Pd) functionalization.

a stable product is reached[19]. Cascades thus offer great advantages in respect of atom economy, and economies of time, labour, resource management and waste generation, and permit the use of synthetically enabling intermediates that may not be practical to isolate. Catalytic cascades, in which the product of a reaction catalysed by species A undergoes a subsequent distinct transformation catalysed by a second species B, are hindered by the possibility of undesired interactions between the initial substrate and the second active site, or indeed between the two catalytic species[20]. Such highly desirable 'one-pot' catalytic cascades therefore necessitate the spatial separation of each catalytic step. The catalytic advantage of spatially segregating Pt NPs within mesopores, accessible overwhelmingly only through interconnected macropores containing Pd NPs, was explored for the cascade oxidative dehydrogenation of cinnamyl alcohol → cinnamaldehyde → cinnamic acid, the last of these an important flavouring and essential oil[21,22]. Pd is highly selective for catalysing cinnamyl alcohol oxidation to cinnamaldehyde[23,24], but promotes decarbonylation of the resultant aldehyde product; in contrast, Pt favours undesired hydrogenation of cinnamyl alcohol (driven by reactively formed surface hydrogen) to 3-phenylpropionaldehyde[25], but is highly selective towards cinnamaldehyde oxidation to the desirable cinnamic acid product[26]. An optimal catalyst design would therefore ensure that cinnamyl alcohol was oxidized over Pd before encountering Pt sites, while permitting the reactively formed cinnamaldehyde to subsequently access Pt sites for the selective production of cinnamic acid in the second oxidation step. Such a goal is achievable only through spatial control over the location of Pd and Pt within a hierarchical catalyst, illustrated schematically in Supplementary Fig. 10, and demonstrated through our catalytic studies below.

Figure 3 summarizes the reaction kinetics (Supplementary Figs 11–14), comparing cinnamyl alcohol conversion and desired cinnamaldehyde and cinnamic acid productivity for our spatially orthogonal PdPt bimetallic catalyst with a variety of monometallic and bimetallic analogues. Monometallic catalysts, their combination as a physical mixture, and conventionally synthesized bimetallic catalysts in which Pd and Pt were co-localized within the hierarchical pore network, proved ineffective, with either low rates of alcohol oxidation, poor selectivity to the cinnamaldehyde intermediate and/or very poor acid production, demonstrating the inability of Pd or Pt to either individually catalyse the cascade reaction, or to communicate effectively when isolated in discrete catalyst support particles. In contrast, their spatial compartmentalization within separate but interconnected pore networks, mere nanometres apart, permits control over the reaction sequence enabling oxidation of cinnamyl alcohol entering the macropores to cinnamaldehyde over Pd, and subsequent aldehyde diffusion into the mesopores and oxidation to cinnamic acid over Pt, conferring an order of magnitude enhancement in cinnamic acid yield. Only selectively functionalized materials in which cinnamyl alcohol was able to react over Pd NPs within macropores, before encountering Pt NPs within mesopores, permit the cascade oxidation.

Localization of different functions within multimodal porous architectures can enhance selectivity in a cascade reaction only if the rate of reactant diffusion is slow relative to the first step in the reaction sequence. Quantitative comparison of our spatially orthogonal bimetallic catalyst with relevant controls evidences that the rate of cinnamyl alcohol selox over Pd indeed exceeds the rate of cinnamyl alcohol diffusion from macropores → mesopores (Supplementary Equation (1)). The benefits of spatially separating the individual oxidation steps was further highlighted through a spiking experiment in which cinnamic acid was directly introduced to the solution mixture at the start of the reaction, enabling

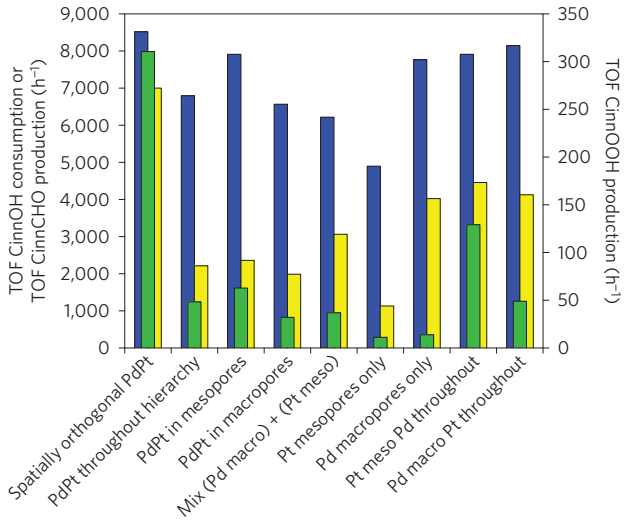

Figure 3 | Reaction dynamics of cinnamyl alcohol oxidation. Active site-normalized rates of cinnamyl alcohol conversion (blue), and cinnamaldehyde (yellow) and cinnamic acid (green) production for the one-pot cascade oxidation of cinnamyl alcohol → cinnamaldehyde → cinnamic acid over a spatially orthogonal, hierarchical Pd macroporous–Pt mesoporous SBA-15 catalyst (1 wt% in each metal), and a range of bimetallic and monometallic SBA-15 analogues including a physical mixture of 1 wt% Pd macroporous and 1 wt% Pd mesoporous SBA-15. Spatially separating the two active sites, and first directing cinnamyl alcohol over Pd, significantly enhances activity and selectivity towards desired selox products. All reactions were performed at 150 °C and 5 bar O_2.

its competitive adsorption with cinnamyl alcohol over Pd within the macropores (Supplementary Fig. 15). Cinnamic acid addition promoted undesired cinnamyl alcohol decarbonylation over Pd at the expense of its selective oxidation to cinnamaldehyde. Spatial separation of the selective oxidation step over Pd that produces cinnamaldehyde, from that over Pt that produces cinnamic acid, and controlling the sequence of these two reactions such that cinnamic acid is formed only after the alcohol has already undergone oxidation to the aldehyde is thus critical to achieving good selox performance. Indeed, our spatially orthogonal bimetallic material outperforms all literature catalysts (Supplementary Table 2) in terms of both turnover frequencies (TOFs) for cinnamyl alcohol oxidation, and selectivity to cinnamaldehyde in high-activity systems, and crucially, is the only heterogeneous catalyst to our knowledge able to produce quantifiable yields of cinnamic acid in a one-pot oxidation of cinnamyl alcohol.

The ability to control the spatial patterning of functionalities within the pore networks of multimodal architectures confers unique and flexible properties on the resulting materials, which are critical to the development of, for example, cascade reactions in which the reaction sequence is controlled by the location of different catalytically active sites. Our methodology is extendable to diverse catalytic cascades featuring chemically incompatible (for example, acid–base[3,27,28]) functions, and, for example, selective functionalization of mesopores and macropores with different fluorescent markers to afford new sensing devices able to discriminate between analytes of different molecular dimensions; macropore and mesopore dimensions are independently tunable, and may be incorporated into different host matrices[29].

Methods

Methods and any associated references are available in the online version of the paper.

Received 4 August 2015; accepted 1 October 2015; published online 16 November 2015

References

1. Parlett, C. M. A., Wilson, K. & Lee, A. F. Hierarchical porous materials: Catalytic applications. *Chem. Soc. Rev.* **42,** 3876–3893 (2013).
2. Climent, M. J., Corma, A., Iborra, S. & Sabater, M. J. Heterogeneous catalysis for tandem reactions. *ACS Catal.* **4,** 870–891 (2014).
3. Merino, E. *et al.* Synthesis of structured porous polymers with acid and basic sites and their catalytic application in cascade-type reactions. *Chem. Mater.* **25,** 981–988 (2013).
4. Balazs, A. C., Emrick, T. & Russell, T. P. Nanoparticle polymer composites: Where two small worlds meet. *Science* **314,** 1107–1110 (2006).
5. Cheong, S. W. & Mostovoy, M. Multiferroics: A magnetic twist for ferroelectricity. *Nature Mater.* **6,** 13–20 (2007).
6. Kim, J., Piao, Y. & Hyeon, T. Multifunctional nanostructured materials for multimodal imaging, and simultaneous imaging and therapy. *Chem. Soc. Rev.* **38,** 372–390 (2009).
7. Maeda, K. *et al.* Photocatalyst releasing hydrogen from water. *Nature* **440,** 295 (2006).
8. Ragesh, P., Ganesh, V. A., Nair, S. V. & Nair, A. S. A review on 'self-cleaning and multifunctional materials'. *J. Mater. Chem. A* **2,** 14773–14797 (2014).
9. Lu, W. & Lieber, C. M. Nanoelectronics from the bottom up. *Nature Mater.* **6,** 841–850 (2007).
10. Zhou, W., Ding, L., Yang, S. & Liu, J. Orthogonal orientation control of carbon nanotube growth. *J. Am. Chem. Soc.* **132,** 336–341 (2010).
11. Paciello, A. & Santonicola, M. G. A supramolecular two-photon-active hydrogel platform for direct bioconjugation under near-infrared radiation. *J. Mater. Chem. B* **3,** 1313–1320 (2015).
12. Chen, A. Y. *et al.* Synthesis and patterning of tunable multiscale materials with engineered cells. *Nature Mater.* **13,** 515–523 (2014).
13. Grunes, J., Zhu, J., Anderson, E. A. & Somorjai, G. A. Ethylene hydrogenation over platinum nanoparticle array model catalysts fabricated by electron beam lithography: Determination of active metal surface area. *J. Phys. Chem. B* **106,** 11463–11468 (2002).
14. Yamada, Y. *et al.* Nanocrystal bilayer for tandem catalysis. *Nature Chem.* **3,** 372–376 (2011).
15. Dhainaut, J., Dacquin, J.-P., Lee, A. F. & Wilson, K. Hierarchical macroporous-mesoporous SBA-15 sulfonic acid catalysts for biodiesel synthesis. *Green Chem.* **12,** 296–303 (2010).
16. Wainwright, S. G. *et al.* True liquid crystal templating of SBA-15 with reduced microporosity. *Micropor. Mesopor. Mater.* **172,** 112–117 (2013).
17. Zhao, D. Y. *et al.* Triblock copolymer syntheses of mesoporous silica with periodic 50 to 300 angstrom pores. *Science* **279,** 548–552 (1998).
18. Mazumder, V. & Sun, S. Oleylamine-mediated synthesis of Pd nanoparticles for catalytic formic acid oxidation. *J. Am. Chem. Soc.* **131,** 4588–4589 (2009).
19. Nicolaou, K. C., Edmonds, D. J. & Bulger, P. G. Cascade reactions in total synthesis. *Angew. Chem. Int. Ed.* **45,** 7134–7186 (2006).
20. Motokura, K., Tada, M. & Iwasawa, Y. Heterogeneous organic base-catalyzed reactions enhanced by acid supports. *J. Am. Chem. Soc.* **129,** 9540–9541 (2007).
21. Burt, S. Essential oils: Their antibacterial properties and potential applications in foods—A review. *Int. J. Food Microbiol.* **94,** 223–253 (2004).
22. Soto-Vaca, A., Gutierrez, A., Losso, J. N., Xu, Z. & Finley, J. W. Evolution of phenolic compounds from color and flavor problems to health benefits. *J. Agric. Food Chem.* **60,** 6658–6677 (2012).
23. Hackett, S. F. J. *et al.* High-activity, single-site mesoporous Pd/Al_2O_3 catalysts for selective aerobic oxidation of allylic alcohols. *Angew. Chem. Int. Ed.* **119,** 8747–8750 (2007).
24. Lee, A. F. *et al.* Reaction-driven surface restructuring and selectivity control in allylic alcohol catalytic aerobic oxidation over Pd. *J. Am. Chem. Soc.* **133,** 5724–5727 (2011).
25. Durndell, L. J. *et al.* Selectivity control in Pt-catalyzed cinnamaldehyde hydrogenation. *Sci. Rep.* **5,** 9425 (2015).
26. Durndell, L. J., Parlett, C. M. A., Hondow, N. S., Wilson, K. & Lee, A. F. Tunable Pt nanocatalysts for the aerobic selox of cinnamyl alcohol. *Nanoscale* **5,** 5412–5419 (2013).
27. Zhang, F., Jiang, H., Li, X., Wu, X. & Li, H. Amine-functionalized GO as an active and reusable acid–base bifunctional catalyst for one-pot cascade reactions. *ACS Catal.* **4,** 394–401 (2014).
28. Zeidan, R. K., Hwang, S.-J. & Davis, M. E. Multifunctional heterogeneous catalysts: SBA-15-containing primary amines and sulfonic acids. *Angew. Chem. Int. Ed.* **45,** 6332–6335 (2006).
29. Dacquin, J.-P. *et al.* An efficient route to highly organized, tunable macroporous-mesoporous alumina. *J. Am. Chem. Soc.* **131,** 12896–12897 (2009).

Acknowledgements
This work was supported by the EPSRC (EP/G007594/4). A.F.L. was supported by an EPSRC Leadership Fellowship, K.W. by a Royal Society Industry Fellowship, and S.K.B. by a Durham University Addison Wheeler Fellowship and The Leverhulme Trust ECF schemes. L.M.B. acknowledges the EPSRC for a studentship. Electron microscopy access was provided through the Leeds EPSRC Nanoscience and Nanotechnology Research Equipment Facility (LENNF) (EP/K023853/1), the University of Birmingham Nanoscale Physics Laboratory, and DU GJ Russell Microscopy Facility.

Author contributions
A.F.L., C.M.A.P. and K.W. planned the experiments. C.M.A.P. synthesized all porous materials and performed catalytic testing. L.M.B. and S.K.B. synthesized and characterized the Pd colloids. C.M.A.P., M.A.I. and N.S.H. undertook materials characterization. A.F.L. wrote the manuscript.

Additional information
Supplementary information is available in the online version of the paper. Reprints and permissions information is available online at www.nature.com/reprints. Correspondence and requests for materials should be addressed to A.F.L.

Competing financial interests
The authors declare no competing financial interests.

Methods

Polystyrene colloidal nanospheres. Monodispersed non-crosslinked polystyrene spheres were produced by adapting literature methods[30]. Styrene (105 cm^3) was washed five times with sodium hydroxide solution (0.1 M, 1:1 vol/vol) followed by five washes with distilled water (1:1 vol/vol) to remove polymerization inhibitors. The washed organic phase was added to nitrogen-degassed water (850 cm^3) at 80 °C followed by dropwise addition of aqueous potassium persulphate solution (0.24 M, 50 cm^3) with 300 r.p.m. agitation. The reaction proceeded for 22 h, after which the solution had turned white owing to the formation of polystyrene nanospheres. Solid product was recovered and colloidal crystal arrangement was induced by centrifugation (Hereus Multifuge X1 with Thermo Fiberlite F15-8x50cy Fixed-Angle Rotor operated at 8,000 r.p.m./7,441*g*, for 1 h). The resulting highly ordered polystyrene colloidal nanosphere crystalline matrix was finally ground to a fine powder for use as the hard macropore-directing template.

Hierarchically ordered SBA-15. The hierarchical, bimodal silica support was synthesized using a modified true liquid crystal templating technique[16] to incorporate the polystyrene nanospheres as macropore-directing hard templates. Pluronic P123 (2 g) was sonicated with hydrochloric acid-acidified water (pH 2, 2 g) at 40 °C to a homogeneous gel. Tetramethoxysilane (4.08 cm^3) was added and stirred rapidly for 5 min at 800 r.p.m. to form a homogeneous liquid. Immediately following this change in physical state the polystyrene colloidal crystals (6 g ground to a fine powder) were added with agitation at 100 r.p.m. for 1 min to homogenize the mix. The resulting viscous mixture was heated under vacuum (100 mbar) at 40 °C to remove the evolved methanol. After 2 h the solid was exposed to the atmosphere at room temperature for 24 h to complete precursor condensation.

Stepwise template extraction and macropore hydrophobization. The preceding parent silica support (10 g) was stirred in toluene (100 cm^3) at −8 °C for 1 min. The solid was recovered by vacuum filtration and briefly washed with cold toluene. The extraction protocol was subsequently repeated four times to fully extract the polystyrene template, affording an empty macropore network without removal of the P123 mesopore template. The resulting solid (2 g) was stirred in triethoxy(octyl)silane (6 cm^3) for 3 min and recovered by vacuum filtration before drying overnight at room temperature. This step introduced hydrophobic character selectivity into the macropores. The macroporous solid (∼2 g) was subsequently refluxed in methanol (400 cm^3) for 18 h to fully extract the Pluronic P123 mesopore-directing agent, and recovered by filtration and washing three times with methanol, to yield a macroporous–mesoporous support with differing hydrophobicity between the interconnected pore networks.

Palladium NP synthesis. Near-monodisperse palladium NPs of 5.6 ± 0.8 nm diameter were prepared by adapting the protocol of ref. 18 to employ a readily available borane complex, and extending the duration of particle ageing at 90 °C to obtain larger NPs. Synthesis was carried out using standard Schlenk techniques under an argon atmosphere. After evacuation of $Pd(acac)_2$ (73 mg, Alfa Aesar) in a 3-neck round-bottom flask and backfilling with Ar (repeated three times), oleylamine (15 cm^3, Acros Organics, 80–90%) was added and the flask heated to 60 °C while stirring. Addition of borane triethylamine (0.52 cm^3, Aldrich, 97%) turned the solution from pale yellow to pale brown and was immediately followed by heating to 90 °C within 15 min, during which time the solution turned black indicating colloidal NP formation. Heating was continued at 90 °C for 90 min before cooling to room temperature. Ethanol (Fisher Scientific, HPLC grade, about 30 cm^3) was added to this suspension, precipitating the NPs, which were then extracted by centrifugation (8,000 r.p.m., 20 min, 50 cm^3 plastic centrifuge tube, prewashed with ethanol). The resulting solid was redispersed in hexane (about 4 cm^3, Fisher Scientific, reagent grade), and the volume of hexane was evaporated to around 2 cm^3 under flowing argon before precipitation by the addition of the minimum quantity of ethanol and separation by centrifugation (6,000 r.p.m., 10 min). Washing in about 2 cm^3 hexane and precipitation with ethanol, followed by centrifugation was repeated a further two times to remove any excess oleylamine and other residual synthetic agents. The solid was finally redispersed and stored in hexane (30 cm^3) until further use. The Pd content of this NP solution was determined by inductively coupled plasma optical emission spectrometry to be 11.0 ± 0.12 mg (in 30 cm^3), indicating that around 43% of the initial Pd is present in the NPs after purification. The as-prepared NPs were characterized by TEM by casting one droplet of NP solution onto a holey carbon-coated copper grid (Agar Scientific) and evaporation to dryness. TEM imaging was performed using a JEOL 2100F FEG TEM with a Schottky field-emission source, equipped with an Oxford INCAx-sight Si(Li) detector for energy-dispersive spectroscopy. The accelerating voltage was 200 kV. The particle size distribution was obtained from imaging 6 different areas of the grid and measuring the diameter over 800 individual NPs. No variation in particle size was apparent in different regions of the grid.

Platinum NP impregnation. Platinum NPs were deposited selectively within the mesopore domains by incipient wetness impregnation of the hydrophobic, hierarchically ordered macroporous–mesoporous SBA-15 with an aqueous solution of dihydrogen hexachloroplatinate. The parent support (0.6 g) was stirred in the aqueous salt solution (3 cm^3, 0.01575 g Pt salt, nominal 1 wt% loading) for 18 h in the dark. A dry powder was obtained by gentle heating of the slurry at 50 °C for 10 h, followed by 100 °C reduction under H_2 (10 cm^3 min^{-1}) for 1 h, yielding monometallic Pt NPs. The bimetallic Pd macropore/Pt mesopore material was produced from the preceding Pt functionalized material (0.3 g) through impregnation with 6.5 cm^3 of a solution of the preformed colloidal Pd NPs in hexane (0.46 mg of Pd NP cm^{-3}, nominal 1 wt% loading). The resulting solid was stirred in solution for 1 h before solvent evaporation at room temperature to leave a dry powder. The monometallic Pd material was produced identically except with omission of the initial aqueous platinum salt impregnation.

Pt and Pd in mesopores. Platinum and palladium NPs were deposited selectively within the mesopore domains by incipient wetness impregnation of the hierarchically ordered macroporous–mesoporous SBA-15, in which the macropores had been previously hydrophobized by triethoxy(octyl)silane, with an aqueous solution of dihydrogen hexachloroplatinate and tetraamine palladium nitrate. The parent support (0.25 g) was stirred in the aqueous salt solution (1 cm^3, 0.0066 g Pt salt and 0.0070 g Pd salt, nominal 1 wt% loading of each) for 18 h in the dark. A dry powder was obtained by gentle heating of the slurry at 50 °C for 10 h, followed by calcination under air at 500 °C for 2 h and subsequent 200 °C reduction under H_2 (10 cm^3 min^{-1}) for 1 h, yielding Pt and Pd NPs.

Pt and Pd in macropores. Platinum and palladium NPs were deposited selectively within the macropore domains by incipient wetness impregnation of macropore template-extracted macroporous–mesoporous SBA-15 (with the mesopores blocked by the Pluronic P123 template) with an aqueous solution of dihydrogen hexachloroplatinate and tetraamine palladium nitrate. The parent support (0.3 g) was stirred in the aqueous salt solution (1 cm^3, 0.0066 g Pt salt and 0.0070 g Pd salt, nominal 1 wt% loading of each) for 18 h in the dark. A dry powder was obtained by gentle heating of the slurry at 50 °C for 10 h, followed by calcination under air at 500 °C for 2 h and subsequent 200 °C reduction under H_2 (10 cm^3 min^{-1}) for 1 h, yielding Pt and Pd NPs.

Pt and Pd in mesopores and macropores. Platinum and palladium NPs were deposited throughout both mesopores and macropores by incipient wetness impregnation of the fully detemplated hierarchically ordered macroporous–mesoporous SBA-15 (in which macropore hydrophobization was omitted) with an aqueous solution of dihydrogen hexachloroplatinate and tetraamine palladium nitrate. The parent support (0.25 g) was stirred in the aqueous salt solution (1 cm^3, 0.0066 g Pt salt and 0.0070 g Pd salt, nominal 1 wt% loading of each) for 18 h in the dark. A dry powder was obtained by gentle heating of the slurry at 50 °C for 10 h, followed by calcination under air at 500 °C for 2 h and subsequent 200 °C reduction under H_2 (10 cm^3 min^{-1}) for 2 h, yielding Pt and Pd NPs.

Pt in mesopores and macropores with Pd in macropores. Platinum NPs were deposited within the mesopore and macropore domains by incipient wetness impregnation of the fully detemplated hierarchically ordered macroporous–mesoporous SBA-15 (in which macropore hydrophobization was omitted) with an aqueous solution of dihydrogen hexachloroplatinate. The parent support (0.25 g) was stirred in the aqueous salt solution (1 cm^3, 0.0066 g Pt salt, nominal 1 wt% loading) for 18 h in the dark. A dry powder was obtained by gentle heating of the slurry at 50 °C for 10 h, followed by 100 °C reduction under H_2 (10 cm^3 min^{-1}) for 2 h, yielding Pt NPs. Pd NPs were selectively deposited within the macropores by impregnation with 5.4 cm^3 of a solution of the preformed colloidal Pd NPs in hexane (0.46 mg of Pd NP cm^{-3}, nominal 1 wt% loading). The solid was stirred in solution for 1 h before solvent evaporation at room temperature to leave a dry powder.

Pd in mesopores and macropores and Pt in mesopores. Platinum NPs were deposited selectively within the mesopore domains by incipient wetness impregnation of the hydrophobic, hierarchically ordered macroporous–mesoporous SBA-15 with an aqueous solution of dihydrogen hexachloroplatinate. The parent support (0.25 g) was stirred in the aqueous salt solution (1 cm^3, 0.0066 g Pt salt, nominal 1 wt% loading) for 18 h in the dark. A dry powder was obtained by gentle heating of the slurry at 50 °C for 10 h, followed by 100 °C reduction under H_2 (10 cm^3 min^{-1}) for 1 h, yielding Pt NPs. The solid was then calcined under air at 500 °C for 2 h to remove the organic octyl groups (hydrophobicity) from the macropores. Palladium NPs were deposited within the mesopore and macropore domains by incipient wetness impregnation with an aqueous solution of tetraamine palladium nitrate. The solid (0.25 g) was stirred in the aqueous salt solution (1 cm^3, 0.0070 g Pd salt, nominal 1 wt% loading) for 18 h. A dry powder was obtained by gentle heating of the slurry at 50 °C for 10 h, followed by calcination under air at 500 °C for 2 h and subsequent 200 °C reduction under H_2 (10 cm^3 min^{-1}) for 2 h, yielding Pt and Pd NPs.

Materials characterization. Nitrogen porosimetry was undertaken on a Quantachrome Autosorb IQTPX porosimeter with analysis using ASiQwin v3.01 software. Samples were degassed at 150 °C for 12 h before recording N_2 adsorption/desorption isotherms. BET surface areas were calculated over the relative pressure range 0.02–0.2. Mesopore properties were calculated applying the BJH (Barrett–Joyner–Halenda) method to the desorption isotherm for relative pressures >0.35, and fitting of isotherms to the relevant DFT (density functional theory) kernel within the software package. Powder X-ray diffraction patterns were recorded using a Bruker D8 diffractometer employing a Cu Kα (1.54 Å) source fitted with a Lynx eye high-speed strip detector. Low-angle patterns were recorded for $2\theta = 0.3°–8°$ with a step size of 0.01°. Wide-angle patterns were recorded for $2\theta = 10°–80°$ with a step size of 0.02°. Contact angle measurements were carried out on a Kruss DSA100 drop shape analyser, fitted with a digital camera for continuous data collection. Water drop shapes were analysed 10 s after deposition using DSA3 software. Thermogravimetric analysis was conducted using a Stanton Redcroft STA 780 thermal analyser at 10 °C min^{-1} under flowing N_2/O_2 (80:20 v/v 20 cm^3 min^{-1}). Scanning electron microscopy (SEM) images were recorded on a Carl ZEISS SUPRA 55-VP operating at 25 kV. Samples were supported on aluminium stubs each backed with carbon tape. Transmission electron microscopy (TEM) imaging of the silica support and preformed Pd NPs was performed using a JEOL 2100F FEG TEM with a Schottky field-emission source, equipped with an Oxford INCAx-sight Si(Li) detector for energy-dispersive spectroscopy (EDX). High-resolution (scanning) transmission electron microscopy (S)TEM images were recorded on either a FEI Tecnai F20 FEG TEM operating at 200 kV equipped with an Oxford Instruments X-Max SDD EDX detector (10 nm diameter spot size), or a JEOL 2100F FEG STEM operating at 200 keV and equipped with a spherical aberration probe corrector (CEOS GmbH) and a Bruker XFlash 5030 EDX. A Hitachi SU8230 cold field-emission SEM operating at 20 kV was used for simultaneous imaging of secondary, backscattered and dark-field scanning transmission electron signals. Samples were prepared for microscopy by dispersion in methanol and drop-casting onto a copper grid coated with a holey carbon support film (Agar Scientific). Images were analysed using ImageJ 1.41 software.

Catalytic cascade oxidation. Catalytic aerobic selective oxidations were performed in a 100 cm^3 Buchi miniclave stirred batch reactor on a 75 cm^3 scale at 150 °C. Catalyst (12.5 mg) was added to reaction mixtures containing 4.2 mmol cinnamyl alcohol (0.562 g), an internal standard (mesitylene, 0.1 cm^3), and toluene solvent (75 cm^3) at 150 °C under 5 bar oxygen and stirring. Reactions were periodically sampled for off-line gas chromatography analysis using a Varian 3800GC with an 8400 autosampler fitted with a CP-Sil5 CB column (15 m × 0.25 mm × 0.25 μm). Conversion, selectivity and yields were calculated through calibration to reference compounds and quoted ±2%. Turnover frequencies for cinnamyl alcohol conversion and cinnamaldehyde production are quoted relative to the surface density of PdO sites (determined by XPS), and for cinnamic acid production relative to the surface density of PtO_2 sites (determined by XPS), being the respective active sites for selective oxidation over Pd NPs and Pt NPs (refs 23,24,26).

References

30. Sen, T., Tiddy, G. J. T., Casci, J. L. & Anderson, M. W. Synthesis and characterization of hierarchically ordered porous silica materials. *Chem. Mater.* **16,** 2044–2054 (2004).